PCCP

PAPER

View Article Online
View Journal | View Issue

Cite this: *Phys. Chem. Chem. Phys.*, 2020, **22**, 489

Three metallic BN polymorphs: 1D multi-threaded conduction in a 3D network†

Mei Xiong,[a] Zhibin Gao,[b] Kun Luo,[c] FeiFei Ling,[c] YuFei Gao,[c] Chong Chen,[a] Dongli Yu,[c] Zhisheng Zhao[c] and Shizhong Wei*[a]

Received 29th October 2019,
Accepted 2nd December 2019

DOI: 10.1039/c9cp05860e

rsc.li/pccp

In this paper, three novel metallic sp^2/sp^3-hybridized boron nitride (BN) polymorphs are proposed by first-principles calculations. One of them, denoted as *t*P-BN, is predicted based on the evolutionary particle swarm structural search. *t*P-BN is composed of two interlocked rings forming a tube-like 3D network. The stability and band structure calculations show that *t*P-BN is metastable and metallic at zero pressure. Calculations for the density of states and electron orbitals confirm that the metallicity originates from the sp^2-hybridized B and N atoms, forming 1D linear conductive channels in the 3D network. According to the relationship between the atomic structure and electronic properties, another two 3D metastable metallic sp^2/sp^3-hybridized BN structures are constructed manually. Electronic property calculations show that both of these structures have 1D conductive channels along different axes. The polymorphs predicted in this study enrich the structures and provide a different picture of the conductive mechanism of BN compounds.

1 Introduction

Boron nitride (BN) compounds have exceptional thermal and chemical stabilities and are widely employed as semiconductors. Experimentally, there are three BN compounds, the bulk sp^3-hybridized structure cubic BN (cBN),[1] wurtzite BN (wBN),[2] and layered sp^2-hybridized hexagonal BN (hBN),[3] respectively. According to the structures of BN allotropes, cBN and wBN can be used as superhard materials, whereas hBN can be used as a lubricant.[3] Recent years have witnessed numerous breakthroughs in BN systems, including novel functional materials' synthesis,[4–15] improvement of physical performance of cBN,[16,17] *etc.* Apart from the three BN compounds which we mentioned above, numerous other BN nanomaterials have been synthesized. For example, zero-dimensional (0D) nanocages,[4,5] one-dimensional (1D) nanotubes,[6–9] two-dimensional (2D) nanosheets,[7,10] and three-dimensional (3D) nanofoams.[11] Furthermore, the Vickers hardness of cBN has been increased to ~100 GPa *via* synthesizing nanotwinned cBN.[18]

Carbon is an isoelectronic structure of the BN structure, and some of the atomic structure and physical property features of the two polymorphs are similar to each other. For example, both bulk cBN and diamond have fully sp^3-hybridized structures and can be used as superhard materials, and the layered hBN and graphite are used as lubricants. However, the electronic properties of these two systems are different. Carbon allotropes can be conductive (such as graphite and synthesized carbon nanotubes)[19] and insulating (such as diamond) depending on their framework. To date, all of the synthesized BN materials have been semiconductors. Both the 1D BN nanotubes and 2D BN nanosheets are wide band-gap semiconductors, independent of their chirality and edges.[20–24] According to these similarities between BN and carbon allotropes, metallic structures might exist in the BN system. Notably, studies showed that some of the bare BNNRs are metals, but this property is unstable, due to the highly active edges.[25–27] Compared to 0D, 1D and 2D structures, 3D bulk structures have distinct advantages in terms of the stability of their physical and chemical properties.

Recently, an increasing number of BN structures have been predicted with the aid of structure search. For example, the superhard *bct*-, *z*-, *p*-BN, the fully sp^2-hybridized 3D networks, and so on.[28–35] All of these structures are semiconductors, and no metals were predicted until 2013. Zhang *et al.*[36] and Dai *et al.*[37] reported metallic BN allotropes in their studies, respectively, which indicate that conductive BN compounds may be synthesized using suitable precursors and methods. Subsequently, Xie *et al.* predicted metallic N-rich B–N compounds.[38] Interestingly, metallic B–N structures possess different conductive mechanisms. For example, in Zhang's work, a conductive network is formed parallel to the (001) crystal surface of T-B_3N_3,[36] whereas in

[a] *National Joint Engineering Research Center for Abrasion Control and Molding of Metal Materials, Henan University of Science and Technology, Luoyang 471003, China. E-mail: hnwsz@126.com*
[b] *Department of Physics, National University of Singapore, Singapore 117551, Republic of Singapore*
[c] *Center for High Pressure Science, State Key Laboratory of Metastable Materials Science and Technology, Yanshan University, Qinhuangdao 066004, China*

† Electronic supplementary information (ESI) available. See DOI: 10.1039/c9cp05860e

Dai's research, both the structures possess 3D conductive networks.[37] These interesting results inspired the metallic structure predictions in the B–N system.

In this work, three novel metastable 3D BN structures are predicted. One of them, denoted *t*P-BN, is predicted by the recently developed *ab initio* evolutionary algorithm CALYPSO, which is helpful for crystal structure prediction studies. The sp^2-hybridized atoms form an interlayer structure, owing to the 1D conduction in the 3D network. Because of the sp^2/sp^3-hybridized structure, the mechanical properties of this metallic structure such as the Vickers hardness and strength are comparable to those of some ceramics. The other two are constructed with sp^2-/sp^3-hybridized atoms, forming a 3D network. The elastic constants meet the criteria for mechanical stability, and phonon frequency calculations demonstrate the dynamical stability. The calculated band structure and density of states suggest the 1D conduction of these novel structures.

2 Computational methods

In this work, the structure search process was performed by the particle swarm optimization methodology implemented by the well-developed CALYPSO (Crystal structure Analysis by Particle Swarm Optimization) code,[39,40] which had been used in many previous studies.[40,41] The calculation was performed assuming zero pressure, and the simulation cell changed from 4 to 30 atoms. Subsequent structural relaxations were conducted using density functional theory (DFT) with the Perdew–Burke–Ernzerhof (PBE) generalized gradient approximation (GGA) and PAW potential, as implemented in the VASP code.[42,43] The used convergence plane-wave cutoff energy was set to 550 eV. The property calculations of the selected structures were performed using the CASTEP code.[44] These included energetic properties, phonon spectra, electronic properties (band structure, projected density of states, and electron orbitals), and mechanical properties (Vickers hardness and tensile strength). The local density approximation (LDA) exchange–correlation function of Ceperley and Alder parameterized by Perdew and Zunger (CA-PZ) was used to describe the electron–electron exchange interaction.[45,46] The cutoff energy and Monkhorst-Pack *k* meshes were carefully chosen to achieve a total energy convergence of 1–2 meV per BN unit. We set the cutoff energy at 770 eV for the norm-conserving (NC) potential. The Monkhorst-Pack *k* meshes of $2\pi \times 0.04$ Å^{-1} separations was chosen for the property calculations. The dynamic stability of the structures was verified by calculating the phonon frequencies through a finite displacement method. Both the LDA functional and Heyd–Scuseria–Ernzerhof hybrid functional (HSE06)[47] were employed to calculate the electronic properties of investigated *t*P-BN. The unit cell was used to calculate the phonon dispersion spectra, electronic properties, the elastic constants, and bulk and shear moduli with 0.003 selected as the applied maximum strain amplitude during the process.

3 Results and discussion

3.1 *t*P-BN structure

3.1.1 Structure characterization. During the structure search, all of the experimental BN allotropes were found, and the previously known BN allotropes were reproduced, such as *bct*-, *p*-BN T-B_3N_3, *etc.*[29,35,36] At zero pressure, the equilibrium lattice parameters of the novel BN structure are $a = b = 2.53$ Å, $c = 9.87$ Å, $\alpha = \beta = \gamma = 90^\circ$, with five B–N pairs per unit cell, assembled in a tetragonal lattice (space group $P\bar{4}m2$, No. 115), denoted as *t*P-BN. Fig. 1 shows the structural feature of *t*P-BN. There are six inequivalent atomic positions in the *t*P-BN framework. Three B atoms, B1, B2 and B3 atoms, occupy the 1b (0.5, 0.5, 0), 2e (0, 0, −0.822), and 2g (0, −0.5, −0.59) position, respectively. Three N atoms, N1, N2 and N3 atoms, occupy the 2g (0, 0.5, −0.09), 2e (0, 0, −0.32), and 1c (0.5, 0.5, 0.5) position, respectively. The B2 and N2 atoms are sp^2-hybridized, whereas the others are sp^3-hybridized. As shown in Fig. 1a, *t*P-BN can be viewed to have 12-atom rings (the red rectangle) interlocked together to form a 3D network in the unit cell.

3.1.2 Stabilities

Thermodynamic stability. To examine the thermodynamic stability, the enthalpies of the *t*P-BN structure are calculated as a function of pressure, and compared with those of several theoretically proposed BN structures, such as *bct*-, *z*-BN, and T-B_3N_3, as depicted in Fig. 2. Accurate structural optimizations were performed for these phases from 0 GPa to 60 GPa. From the energetic point of view, *t*P-BN is found to be metastable as compared to the proposed semiconductor *bct*-BN, *p*-BN, and metallic M-BN, but energetically more stable than the previously proposed metallic T-B_3N_3 structure, at zero as well as high pressures.

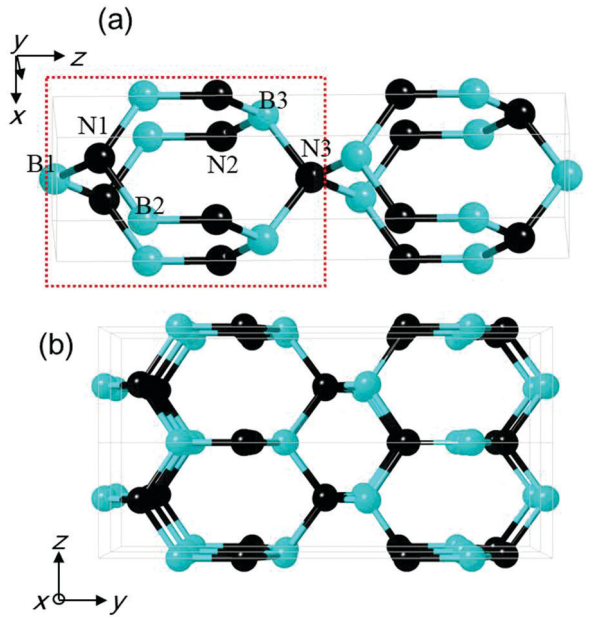

Fig. 1 Atomic configurations of *t*P-BN. (a) Top view and (b) perspective view. The cyan and black balls stand for B and N atoms, respectively.

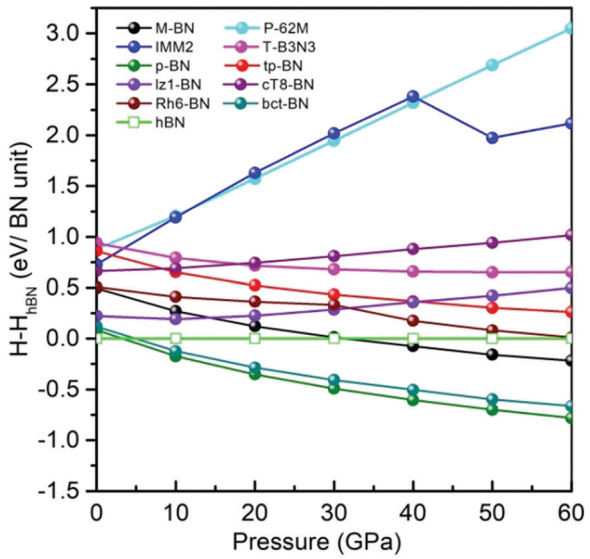

Fig. 2 Calculated enthalpies of BN structures relative to hBN as a function of pressure.

Dynamic stability. To evaluate the dynamic stability of *t*P-BN, we investigate the phonon dispersion and frequency density of states (DOS) in the first Brillouin zone at zero pressure. The coordinates of the high symmetry point sequence in reciprocal space are $Z\,(0, 0, 0.5) \rightarrow A\,(0.5, 0.5, 0.5) \rightarrow M\,(0.5, 0.5, 0.0) \rightarrow G\,(0, 0, 0) \rightarrow Z\,(0, 0, 0.5) \rightarrow R\,(0, 0.5, 0.5) \rightarrow X\,(0, 0.5, 0) \rightarrow G\,(0, 0, 0)$. As plotted in Fig. 3a, we find that there are no imaginary frequencies in the whole Brillouin zone, which indicates that *t*P-BN is dynamically stable. The highest calculated phonon frequency of bond vibrational modes in *t*P-BN is 38.1 THz, a significant phonon gap departs the whole dispersion into two parts, the low frequency (0–33.3 THz) and the high frequency (37.9–38.1 THz) regions. According to the phonon DOS results shown in Fig. 3b, the high-frequency modes are entirely contributed by the B2 and N2 atoms, while the partial DOS of sp^3-hybridized atoms and total DOS overlap in the low-frequency region.

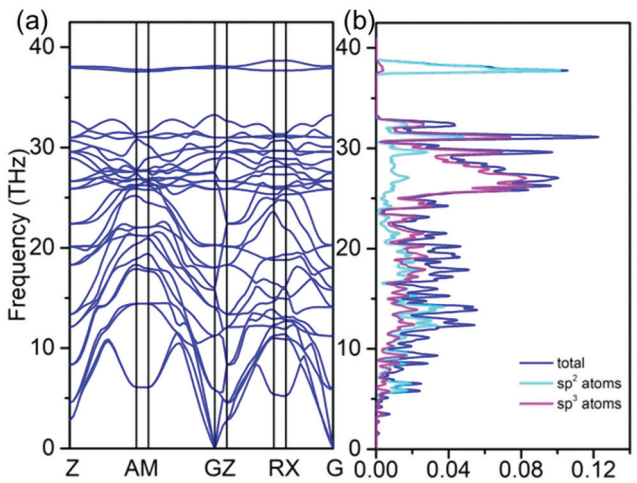

Fig. 3 Phonon dispersion (a) and frequency DOS (THz^{-1}) of *t*P-BN.

Mechanical stability. The mechanical stability is investigated by elastic constant calculations. The results are: C_{11} = 709.2, C_{33} = 928.0, C_{44} = 177.0, C_{66} = 127.5, C_{12} = 68.6 and C_{13} = 138.0 GPa, respectively. For a stable tetragonal structure, all six independent elastic constants should meet the generalized Born stability criteria:[48] $C_{11} > 0$, $C_{33} > 0$, $C_{44} > 0$, $C_{66} > 0$, $C_{11} - C_{12} > 0$, $C_{11} + C_{33} - 2\,C_{13} > 0$, $2\,(C_{11} + C_{12}) + C_{33} + 4\,C_{13} > 0$. These elastic constants satisfy the criteria, which indicate that *t*P-BN is mechanically stable. The calculated bulk modulus is 332.9 GPa, indicating that *t*P-BN is more compressible than cBN (400 GPa).[49]

3.1.3 Mechanical properties

Strength. To study the mechanical properties of the *t*P-BN structure, the tensile strength and theoretical Vickers Hardness are calculated. According to the tetragonal crystal structure of *t*P-BN, we choose the [100], [001], and [110] directions to determine the ideal tensile strength. As shown in Fig. 4, the strength is investigated for different percentages (5%, 10%, 15%, 20%...60%) of tensile strains. The calculated tensile strengths along [100], [001] and [110] are 66.47 GPa with a strain of 0.25, 125.86 GPa with a strain of 0.2, and 147.5 GPa with a strain of 0.55, respectively. Apparently, these results manifest the anisotropy of the tensile strengths of *t*P-BN. The [110] tensile strength of 147.5 GPa is comparable to the in-plane tensile strength of graphene (130 ± 10 GPa).[50] The weakest tensile strength is along the [100] direction, which indicates that the crystal will cleave along the [100] direction as soon as the external stress exceeds 66.47 GPa.

Vickers hardness. Generally, the theoretical Vickers Hardness of structures can be calculated with the microscopic model and empirical formula reported by Tian *et al.*[51,52] and Chen *et al.*,[53] respectively. Considering the sp^2-hybridized atoms and tube-like features of the *t*P-BN framework, the theoretical Vickers Hardness is calculated using the empirical formula. The formula is depicted

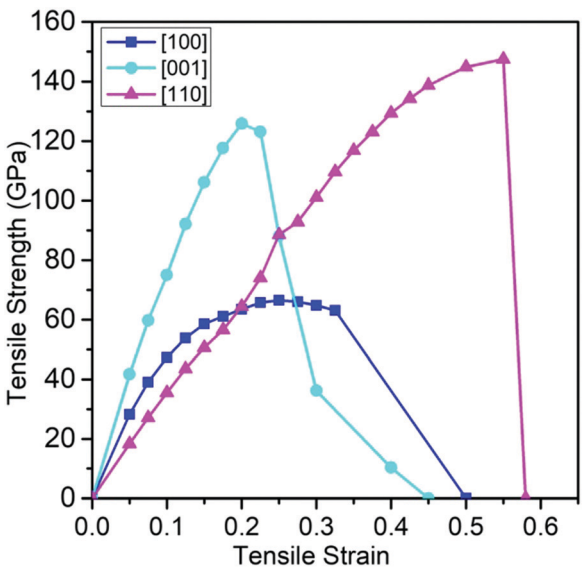

Fig. 4 Calculated tensile strengths *versus* tensile strains of *t*P-BN along the [100], [001], and [110] directions, respectively.

as: H_v (GPa) = $2(G^3/B^2)^{0.585} - 3$. The calculated bulk modulus (B), shear modulus (G) and Young's modulus (E) of the *t*P-BN structure are 332.9 GPa, 214.0 GPa and 528.7 GPa, respectively. Consequently, the calculated Vickers Hardness value is 24.5 GPa, which is comparable to that of Al_2O_3 (~20 GPa)[54] ceramic, implying that *t*P-BN is a hard material.

3.1.4 Electronic properties. The electronic properties of *t*P-BN are studied by calculating its band structure, and the results are shown in Fig. 5. The high symmetry *K*-point path of band calculation we chose in the Brillouin zone is the same as that used in the phonon calculation. Firstly, the band structure calculated with DFT calculations is plotted with red lines in Fig. 5a. The results show that there are three partially occupied bands crossing the Fermi level in the Brillouin zone, indicating the metallic feature of *t*P-BN. However, DFT calculations are well-known to underestimate the band gap.[55] In terms of deriving a more accurate band structure, the screened hybrid functional HSE06 has been demonstrated to be more credible than DFT calculations. Thus, we re-calculated the band structure with the HSE06 functional, and the results are depicted in Fig. 5a, marked with blue lines. One can see that there are two partially occupied bands crossing the Fermi level, which confirms the inherent metallicity of *t*P-BN.

As revealed in previous studies, metallic BN structures possess a unique conductive mechanism depending on their atomic framework.[36–38] The origin of metallicity requires further exploration, thus we first calculated the density of states (DOS) and projected density of states (PDOS) of *t*P-BN and plotted the results in Fig. 5b. As shown in Fig. 5b, the contributions at the Fermi level originated from the p orbitals of these atoms. Moreover, as shown in Fig. 5c–e, most of the electron states at the Fermi level are contributed by the p orbitals of N2 and B2 atoms, and the contributions from B2 atoms are smaller than that from N2 atoms. To further study the conductive mechanism, we calculated the electron orbitals of *t*P-BN, and plotted the results in Fig. 5f and g. The drawn electron orbitals are the summation of the partially occupied bands crossing the Fermi level. As shown in Fig. 5f the sp^2-hybridized B2 and N2 atoms formed a layered configuration along the *x*- and *y*-axis, respectively. In the left part of Fig. 5f, the orbitals of N2 atoms overlapped along the *y*-axis and the orbitals of B2 atoms overlapped along the *x*-axis. The geometries in the right parts are opposite to those on the left, namely the orbitals of N2 atoms overlapped along the *x*-axis, and the orbitals of B2 atoms overlapped along the *y*-axis. Moreover, as shown in Fig. 5g, the conductive channels are separated from each other. This indicates that *t*P-BN is linearly conductive, with independent conductive channels in its framework, *i.e.*, a 3D BN network with peculiar 1D dual-threaded conductivity. This revealed conductive mechanism is different from the previously predicted metallic BN structures, such as T-B_3N_3 which has a 2D conductive network;[36] the structures predicted by Dai have a 3D network,[37] and *t*-B_3N_4 has a 2D conductive network.[38]

3.2 Manual construction of metallic BN structures

3.2.1 Structure construction. The proposed metallic B–N structures demonstrate that the well-semiconductor BN can achieve metallicity depending on the atomic configuration.[36–38] Due to the hybridization diversity of B and N atoms, some other

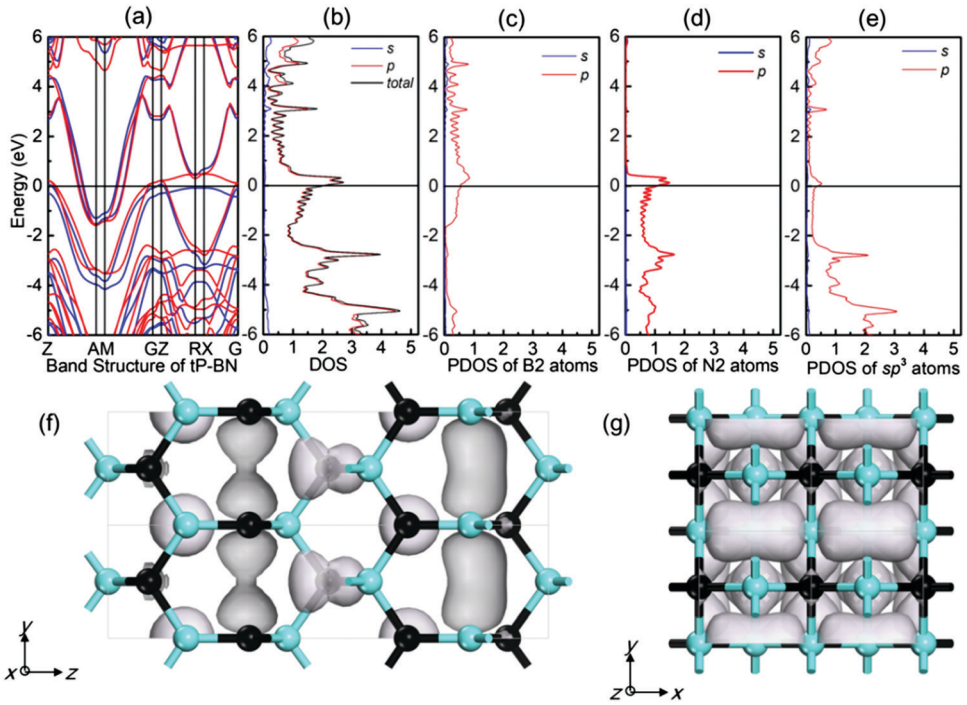

Fig. 5 Electronic properties of *t*P-BN. (a) Band structure, (b) the density of states, (c)–(e) projected density of states, and (f)–(g) electron orbitals of *t*P-BN across the Fermi level. The selected isosurface is 0.04. The cyan and black balls stand for B and N atoms, respectively.

metallic structures may exist in the B–N system. In terms of the structure configuration, several similarities exist among T-B_3N_3, (P-6M2)-BN, (IMM2)-BN and *t*-B_3N_4, which include sp^2-hybridized atoms, flat layers and a smaller interlayer distance (~2.6 Å) than hBN (~3.33 Å) to form a tube-like 3D network. Moreover, both *t*P-BN and T-B_3N_3 have interlocked rings that form a tube-like 3D structure. Therefore, we have constructed several BN structures by adding sp^2-hybridized B–N pairs based on the *t*P-BN framework, forming a tube-like 3D network to search metallic BN polymorphs. As a result, two metastable BN structures have been obtained at zero pressure, denoted as B_8N_8-I and B_8N_8-II, respectively. Under zero pressure, the equilibrium lattice parameters of the B_8N_8-I structure are $a = b = 2.55$ Å, and $c = 15.86$ Å, with four B and four N atoms per unit cell, assembled in a tetragonal lattice (space group *P*42*mc*, no. 105), and the atomic positions are listed in Table S1 (see the ESI†). We have plotted the frameworks of B_8N_8-I in Fig. 6a and b. As shown in Fig. 6a, similarly to *t*P-BN, B_8N_8-I is composed of the interlocked blocks marked with the red frame. Fig. 6b shows the sp^2/sp^3 hybridized features of B_8N_8-I, and the sp^2 hybridized atoms (B2, B3, N2, and N3) and sp^3-hybridized atoms (B1, B4, N1, and N4). Thereafter, by switching the atomic positions of B and N atoms in the B_8N_8-I structure, we obtained another framework, denoted as B_8N_8-II, shown in Fig. 6c and d.

3.2.2 Stability. We tested the thermodynamic stability by calculating the total energy at zero pressure. The results show that B_8N_8-I and B_8N_8-II structures are ~0.22 eV per BN unit lower than that of *t*P-BN. Therefore, at zero pressure, the constructed B_8N_8-I and B_8N_8-II structures are thermodynamically more stable than *t*P-BN. The dynamic stability of the B_8N_8-I and B_8N_8-II structures is investigated *via* the phonon dispersion calculations at zero pressure, and the results are shown in Fig. S1 (see the ESI†). The coordinates of the high symmetry point sequence in the first Brillouin zone are the same as those of *t*P-BN. As shown in Fig. S1a and b (ESI†), there are no imaginary frequencies in the whole Brillouin zone, which means that the two structures are dynamically stable. The mechanical stability of the two structures is investigated by elastic constant calculations, and the results are listed in Table S2 (see the ESI†). These elastic constants satisfy the criteria for a stable tetragonal structure, which indicate that both B_8N_8-I and B_8N_8-II are mechanically stable.

3.2.3 Electronic properties. In order to study the electronic properties of the two structures B_8N_8-I and B_8N_8-II, the band structures and PDOS are calculated. As we mentioned above, the band structure is calculated by the HSE06 and LDA functional, respectively, to obtain reliable results (see Fig. S2a and b in the ESI†). In Fig. S2a and b (ESI†), the blue lines stand for the results calculated by the LDA functional, and the red lines depict the results derived by the HSE06 functional. As shown by previous studies, the band crossing the Fermi level and the obvious density of state peak at the Fermi level indicate the metallic feature of crystal structures.[56,57] Fig. S2a (ESI†) shows the band structure and DOS of B_8N_8-I. Four partially occupied bands crossing the Fermi level in the Brillouin zone (blue line) are observed, indicating the metallic feature of B_8N_8-I. In the DOS of B_8N_8-I, the occupations at Fermi level can be observed, which is consistent with the result we derived from the band structure. The similar results can be observed in Fig. S2b (ESI†), which shows the band structure and DOS of B_8N_8-II. There are six partially occupied bands crossing the Fermi level in the band structure (blue line), and an obvious density of state peak at the Fermi level in the DOS, which indicate the metallic feature. For the B_8N_8-I structure, the PDOS curves in Fig. S2c (see the ESI†) show that occupations at the Fermi level are mainly contributed by the sp^2-hybridized B3, N2 and N3 atoms. For the B_8N_8-II structure, the partial DOS curves in Fig. S2d (see the ESI†) show that most of the occupations at the Fermi level are contributed by the sp^2-hybridized N3, B2 and B3 atoms.

The electron orbitals originating from the bands across the Fermi level of these two structures are also calculated to investigate the conductive mechanism. As shown in Fig. 6, each

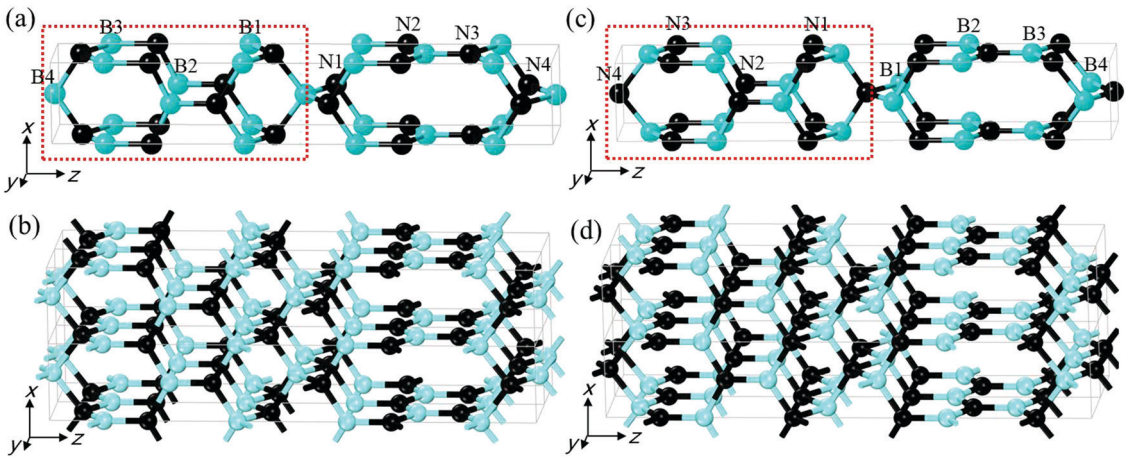

Fig. 6 Structure configurations of constructed metallic BN structures. (a) and (b) B_8N_8-I and (c) and (d) B_8N_8-II. The cyan and black balls stand for B and N atoms, respectively.

of the two structures can be divided into two parts, the left part including the atoms in the red frame, and the right part including the remaining atoms. The calculated results for electron orbitals of B_8N_8-I originating from the bands across the Fermi level are shown in Fig. 7a and b. In the left part of Fig. 7a, the electron orbitals of the sp^2-hybridized B3 atoms overlapped along the *x*-axis, which originated from the delocalized π electrons of B3-p orbitals. Similarly, the overlapped electron orbitals of sp^2-hybridized N3 atoms can be seen between the N3 layers along the *y*-axis. Fig. 7b shows the details of the blue frame in Fig. 7a, in which we can observe that the electron orbitals of sp^2-hybridized N2 atoms are connected together along the N2–B2–N2 chain. The electron orbitals of the right part we calculated can be viewed as rotating the left part with 90°. That is the conductive channel formed by B3, N2 and N3 atoms is along the *y*-axis, N2–B2–N2 chain and *x*-axis, respectively.

The underlying conductive mechanism is owing to the short interlayer distance between the sp^2-hybridized atoms along the axis. For example, the interlayer distance of B3 atoms is 2.56 Å, which is much smaller than the layer separation in the hBN structure (~3.33 Å). Therefore, the π interactions between B3 atoms are enhanced and formed conductive channels. Moreover, the π electrons of B2 atoms are restricted by N2 and N3 atoms with the stronger electronegativity, inducing no π-like interactions between B2 atoms even if with a small interlayer separation. These results are consistent with the analyses of PDOS.

The conductive mechanism of the B_8N_8-II structure is similar to that of the B_8N_8-I structure. As shown in Fig. 7c, for the left part of B_8N_8-II, owing to the short interlayer distance (~2.56 Å), the π electrons of sp^2-hybridized N3, B2 and B3 atoms made their p orbitals overlap along *x*-, *y*- and *y*-axis, respectively. Fig. 7d shows the details of the section in the blue frame of Fig. 7c. It shows that the three conductive channels are independent, none of them are overlapped. In the right part, the electron orbitals of N3, B2 and B3 atoms overlapped along the *y*-, *x*- and *x*-axis, respectively. Similarly, the three conductive channels also isolated from each other. However, there are no electron orbitals overlapping between the sp^2-hybridized N2 atoms. This might be caused by the unique crystal configuration, which is the N1-B3 bonds restricted the electrons of N2 atoms.

All of the three novel BN polymorphs have 1D conductive channels in their 3D network, the differences between them lie in the counts of conductive channels, which are caused by the crystal structure. In previous studies, the results show the electronic properties of structures depending on the atomic configurations.[56,57] For example, the (3,3) BNT has four conductive channels, whereas (5,0) BNT has three conductive channels.[56] What's more, the metal–semiconductor transition can be induced by the distorted B atoms.[56] In this work, there are three, four and six partially occupied bands crossing the Fermi level in the Brillouin zone of *t*P-BN, B_8N_8-I and B_8N_8-II, respectively. Moreover, there are four conductive channels in *t*P-BN, whereas there are six conductive channels in B_8N_8-I and B_8N_8-II, respectively. With the addition of sp^2-hybridized atoms, the counts of conductive channel increase correspondingly, and the electron distributions are changed according to the configurations of these sp^2-hybridized atoms.

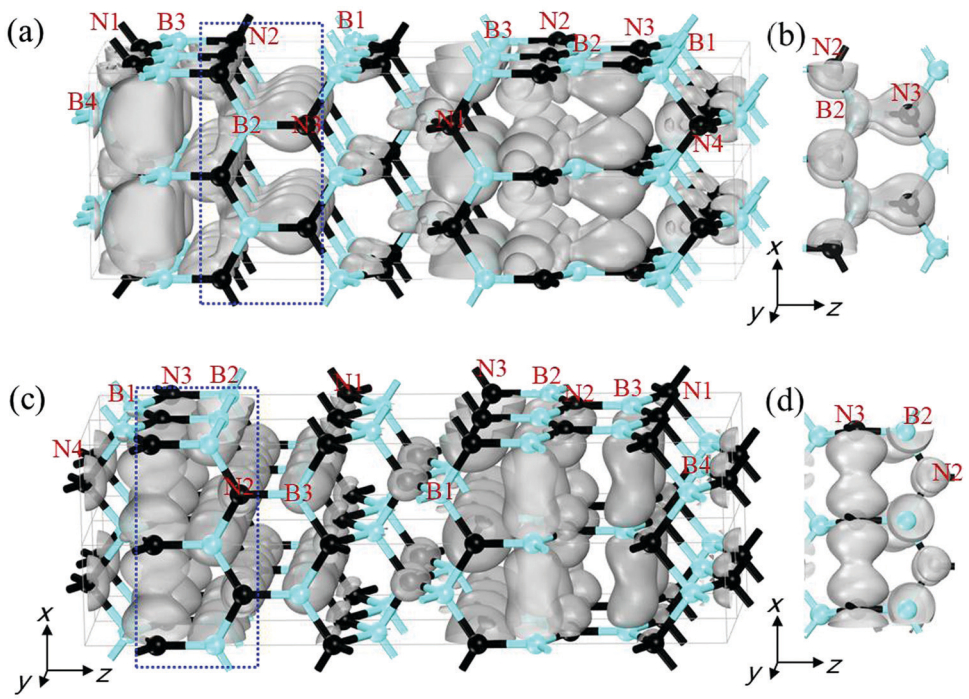

Fig. 7 Electron orbitals of (a) and (b) B_8N_8-I, and (c) and (d) B_8N_8-II across the Fermi level. The selected isosurface is 0.033. The cyan and black balls stand for B and N atoms, respectively.

4. Conclusions

In summary, three metastable sp^2/sp^3-hybridized BN polymorphs are proposed as metallic frameworks and are demonstrated to be mechanically and dynamically stable at zero pressure. Structurally, these three BN structures possess a tetragonal unit cell with interlocked units to form a tube-like configuration. The band structure, DOS and electron orbital calculations show that sp^2-hybridized B and N atoms in these structures constitute independent 1D multi-threaded conductive channels along the *x*- and *y*-axis, respectively. These results indicate that the sp^2/sp^3-hybridized BN structure with interlocked units can be taken into consideration during the BN metallic structure search. The electronic properties of three BN structures demonstrate the diversity of the conductive mechanism of metallic BN and indicate their potential applications in electronic devices.

Conflicts of interest

There are no conflicts to declare.

Acknowledgements

This work is supported by the open science and technology cooperation of Henan province China (No. 182106000024).

References

1 R. H. Wentorf Jr, *J. Chem. Phys.*, 1957, **26**, 956.
2 F. P. Bundy and R. H. Wentorf, *J. Chem. Phys.*, 1963, **38**, 1144.
3 Y. Kimura, T. Wakabayashi, K. Okada, T. Wada and H. Nishikawa, *Wear*, 1999, **232**, 199–206.
4 D. Golberg, Y. Bando, O. Stephan and K. Kurashima, *Appl. Phys. Lett.*, 1998, **73**, 2441–2443.
5 O. Stephan, Y. Bando, A. Loiseau, F. Willaime, N. Shramchenko, T. Tamiya and T. Sato, *Appl. Phys. A: Mater. Sci. Process.*, 1998, **67**, 107–111.
6 N. G. Chopra, R. J. Luyken, K. Cherrey, V. H. Crespi, M. L. Cohen, S. G. Louie and A. Zettl, *Science*, 1995, **269**, 966–967.
7 D. Golberg, Y. Bando, Y. Huang, T. Terao, M. Mitome, C. Tang and C. Zhi, *ACS Nano*, 2010, **4**, 2979–2993.
8 A. Rubio, J. L. Corkill and M. L. Cohen, *Phys. Rev. B: Condens. Matter Mater. Phys.*, 1994, **49**, 5081.
9 B. Santra, H.-Y. Ko, Y.-W. Yeh, F. Martelli, I. Kaganovich, Y. Raitses and R. Car, *Nanoscale*, 2018, **10**, 22223–22230.
10 D. Pacile, J. C. Meyer, Ç. Girit and A. Zettl, *Appl. Phys. Lett.*, 2008, **92**, 133107.
11 S. Chatterjee, M. J. Kim, D. N. Zakharov, S. M. Kim, E. A. Stach, B. Maruyama and L. G. Sneddon, *Chem. Mater.*, 2012, **24**, 2872–2879.
12 A. Rendón-Patiño, A. Doménech, H. García and A. Primo, *Nanoscale*, 2019, **11**, 2981–2990.
13 R. Kumar and A. Parashar, *Nanoscale*, 2016, **8**, 22–49.
14 V. Yadav and V. Kulshrestha, *Nanoscale*, 2019, **11**, 12755–12773.
15 D. H. Suh, *Nanoscale*, 2014, **6**, 5686–5690.
16 N. Dubrovinskaia, V. L. Solozhenko, N. Miyajima, V. Dmitriev, O. O. Kurakevych and L. Dubrovinsky, *Appl. Phys. Lett.*, 2007, **90**, 101912.
17 V. L. Solozhenko, O. O. Kurakevych and Y. Le Godec, *Adv. Mater.*, 2012, **24**, 1540–1544.
18 Y. Tian, B. Xu, D. Yu, Y. Ma, Y. Wang, Y. Jiang, W. Hu, C. Tang, Y. Gao, K. Luo, Z. Zhao, L. M. Wang, B. Wen, J. He and Z. Liu, *Nature*, 2013, **493**, 385–388.
19 A. Thess, R. Lee, P. Nikolaev, H. Dai, P. Petit, J. Robert, C. Xu, Y. H. Lee, S. G. Kim and A. G. Rinzler, *Science*, 1996, **273**, 483–487.
20 X. Blase, A. Rubio, S. G. Louie and M. L. Cohen, *EPL*, 1994, **28**, 335.
21 K. H. Khoo and S. G. Louie, *Phys. Rev. B: Condens. Matter Mater. Phys.*, 2004, **69**, 201401.
22 H. Zeng, C. Zhi, Z. Zhang, X. Wei, X. Wang, W. Guo, Y. Bando and D. Golberg, *Nano Lett.*, 2010, **10**, 5049–5055.
23 X. Li, J. Yin, J. Zhou and W. Guo, *Nanotechnology*, 2014, **25**, 105701.
24 Y. Xue, Q. Liu, G. He, K. Xu, L. Jiang, X. Hu and J. Hu, *Nanoscale Res. Lett.*, 2013, **8**, 49.
25 E. Kan, F. Wu, H. Xiang, J. Yang and M.-H. Whangbo, *J. Phys. Chem. C*, 2011, **115**, 17252–17254.
26 M. Wu, X. Wu, Y. Pei and X. C. Zeng, *Nano Res.*, 2011, **4**, 233–239.
27 F. Zheng, G. Zhou, Z. Liu, J. Wu, W. Duan, B.-L. Gu and S. B. Zhang, *Phys. Rev. B: Condens. Matter Mater. Phys.*, 2008, **78**, 205415.
28 C. He, L. Sun, C. Zhang, X. Peng, K. Zhang and J. Zhong, *Phys. Chem. Chem. Phys.*, 2012, **14**, 10967.
29 B. Wen, J. Zhao, R. Melnik and Y. Tian, *Phys. Chem. Chem. Phys.*, 2011, **13**, 14565.
30 J. Dai, X. Wu, J. Yang and X. C. Zeng, *J. Phys. Chem. Lett.*, 2014, **5**, 393–398.
31 Q. Fan, Q. Wei, H. Yan, M. Zhang, Z. Zhang, J. Zhang and D. Zhang, *Comput. Mater. Sci.*, 2014, **85**, 80–87.
32 C.-Y. Niu and J.-T. Wang, *Phys. Lett. A*, 2014, **378**, 2303–2307.
33 G. Yang and B. F. Chen, *J. Alloys Compd.*, 2014, **598**, 54–56.
34 Z. Zhang, M. Lu, L. Zhu, L. Zhu, Y. Li, M. Zhang and Q. Li, *Phys. Lett. A*, 2014, **378**, 741–744.
35 J. Long, C. Shu, L. Yang and M. Yang, *J. Alloys Compd.*, 2015, **644**, 638–644.
36 S. Zhang, Q. Wang, Y. Kawazoe and P. Jena, *J. Am. Chem. Soc.*, 2013, **135**, 18216–18221.
37 J. Dai, X. Wu, J. Yang and X. C. Zeng, *J. Phys. Chem. Lett.*, 2013, **4**, 3484–3488.
38 C. Xie, M. Ma, C. Liu, Y. Pan, M. Xiong, J. He, G. Gao, D. Yu, B. Xu and Y. Tian, *J. Mater. Chem. C*, 2017, **5**, 5897–5901.
39 Y. Wang, J. Lv, L. Zhu and Y. Ma, *Comput. Phys. Commun.*, 2012, **183**, 2063–2070.
40 Y. Wang, J. Lv, L. Zhu and Y. Ma, *Phys. Rev. B: Condens. Matter Mater. Phys.*, 2010, **82**, 094116.

41 Q. Wang, B. Xu, J. Sun, H. Liu, Z. Zhao, D. Yu, C. Fan and J. He, *J. Am. Chem. Soc.*, 2014, **136**, 9826–9829.
42 P. E. Blöchl, *Phys. Rev. B: Condens. Matter Mater. Phys.*, 1994, **50**, 17953.
43 G. Kresse and J. Furthmüller, *Phys. Rev. B: Condens. Matter Mater. Phys.*, 1996, **54**, 11169.
44 S. J. Clark, M. D. Segall, C. J. Pickard, P. J. Hasnip, M. I. J. Probert, K. Refson and M. C. Payne, *Z. Kristallogr. – Cryst. Mater.*, 2005, **220**, 567–570.
45 J. P. Perdew and A. Zunger, *Phys. Rev. B: Condens. Matter Mater. Phys.*, 1981, **23**, 5048.
46 D. M. Ceperley and B. J. Alder, *Phys. Rev. Lett.*, 1980, **45**, 566.
47 J. Heyd, G. E. Scuseria and M. Ernzerhof, *J. Chem. Phys.*, 2003, **118**, 8207–8215.
48 Z.-j. Wu, E.-j. Zhao, H.-p. Xiang, X.-f. Hao, X.-j. Liu and J. Meng, *Phys. Rev. B: Condens. Matter Mater. Phys.*, 2007, **76**, 054115.
49 M. Grimsditch, E. S. Zouboulis and A. Polian, *J. Appl. Phys.*, 1994, **76**, 832–834.
50 C. Lee, X. Wei, J. W. Kysar and J. Hone, *Science*, 2008, **321**, 385–388.
51 J. He, E. Wu, H. Wang, R. Liu and Y. Tian, *Phys. Rev. Lett.*, 2005, **94**, 015504.
52 F. Gao, J. He, E. Wu, S. Liu, D. Yu, D. Li, S. Zhang and Y. Tian, *Phys. Rev. Lett.*, 2003, **91**, 015502.
53 X.-Q. Chen, H. Niu, D. Li and Y. Li, *Intermetallics*, 2011, **19**, 1275–1281.
54 R. A. Andrievski, *Int. J. Refract. Met. Hard Mater.*, 2001, **19**, 447–452.
55 Z. Gao, Z. Zhou and D. Tománek, *ACS Nano*, 2019, **13**, 5103–5111.
56 X. Dai, L. Zhang, J. Li and H. Li, *J. Phys. Chem. C*, 2017, **121**, 26096–26101.
57 X. Dai, L. Zhang, J. Li, Z. Wang and H. Li, *J. Mater. Chem. C*, 2018, **6**, 5794–5802.

